RESEARCH ARTICLE

small methods
www.small-methods.com

CMOS-Compatible Protonic Three-Terminal Memristor for Analog Synapse in Neuromorphic Computing

*Lingli Liu, Putu Andhita Dananjaya, Eng Kang Koh, Funan Tan, Ze Chen, Gerard Joseph Lim, Calvin Xiu Xian Lee, Jin-Lin Yang, and Wen Siang Lew**

All-solid-state inorganic hydrogen-based three-terminal memristors (H-3TMs) suffer from poor retention, susceptibility to humidity and temperature, and the reliance on wet chemistry during fabrication, hindering their manufacturability within existing foundry processes. To address these, this study presents a CMOS-compatible H-3TM based on reversible intercalation and extraction of protons between the SiN_x electrolyte and WO_x channel. The protons are introduced via a straightforward hydrogen plasma treatment, promoting a compatible fabrication process with back-end-of-line integration. Experimental and simulation results indicate that the low proton transport tendency across the electrolyte/channel interface without an external electric field contributes to high retention performance. Furthermore, the device demonstrates linear potentiation and depression, 512 conductance states with a dynamic range of ≈40, low energy operation (≈73 fJ per write), and excellent overall device-to-device variation. Its analog properties are evaluated under the training and inference framework of MNIST and Fashion-MNIST datasets. The device achieved training and inference accuracies only 0.4% and 0.3% below the ideal benchmark on the F-MNIST dataset. This work offers a rational approach for future artificial synaptic device design and fabrication.

1. Introduction

Three-terminal memristor (3TM) capable of multi-level memory storage has emerged as a promising candidate for implementing artificial synapses in neuromorphic computing systems.[1–4] A 3TM consists of a channel layer sandwiched between source and drain electrodes and an electrolyte layer. Electrolytes in the 3TMs contain active mobile ions that are ready to move upon the application of a bias to a separate gate terminal. This gate bias leads to the injection of active ions into the channel, thereby precisely adjusting the channel conductance through electrochemical reactions.[5,6] This mode of operation allows a linear and symmetric conductance modulation behavior under identical pulse schemes. Thus, 3TMs offer a more robust synaptic operation than the reported two-terminal counterparts, e.g., resistive random-access memory and phase-change memory.[7–10]

In 3TMs, H^+ (proton), Li^+, and O^{2-} are typically employed as the active mobile ions. Li-3TMs feature fast switching and high endurance, but the potential risk of silicon device contamination cannot be ignored.[11–14] O^{2-}, due to its inherently slow motion, requires a long pulse duration to function under room temperature, despite its well-established complementary metal-oxide semiconductor (CMOS) compatibility characteristics.[15–17] Compared to Li^+ and O^{2-}, a proton has a much smaller radius that not only guarantees rapid switching capabilities but also offers high compatibility with CMOS technology. Therefore, H-3TMs are strongly regarded as the optimal candidates for synaptic devices.[18,19] However, the implementation challenges of H-3TMs lie in their low retention and complicated proton incorporation process.

Among the reported CMOS-compatible H-3TMs, only palladium (Pd), WO_3, SiO_2, and Si have been utilized as proton reservoirs so far.[18,20,21] Specifically, the hydrogenation of Pd is realized by exposing it to forming gas that contains H_2. However, the hydrogenated PdH_x is vulnerable to air and moisture, which requires an enclosed chamber filled with forming gases when conducting electrical characterization. A Pd-based H-3TM device demonstrates the smallest dimension of 100 nm and a nanosecond-level switching speed, however, it shows a limited retention of 100 s.[21] More recently, a hydrogen spillover process has been applied to form a hydrogenated WO_3 reservoir.[7] This spillover involves a wet etching process, and it can achieve wafer-scale proton doping. Nevertheless, to reach an ideal base channel conductance (in nano- to micro-siemens), a post-annealing process is required to tune the hydrogen concentration in the channel. Another study shows that annealing in H_2 can implant protons into the Si reservoir layer, and the Si—H bonds are fragile under the applied electric field, allowing protons to infuse into the device. However, the effect of this doping method is limited, as indicated by the small dynamic range of the device.[19,22] Therefore, for H-3TM devices, a more facile hydrogen introduction method

L. Liu, P. A. Dananjaya, E. K. Koh, F. Tan, Z. Chen, G. J. Lim, C. X. X. Lee, J.-L. Yang, W. S. Lew
School of Physical and Mathematical Sciences
Nanyang Technological University
Singapore 637371, Singapore
E-mail: wensiang@ntu.edu.sg

The ORCID identification number(s) for the author(s) of this article can be found under https://doi.org/10.1002/smtd.202500445

DOI: 10.1002/smtd.202500445

is required. Additionally, the fast transportation of protons leads to retention issues, so the retention performance must also be considered when developing H-3TMs.

Hydrogen plasma has been widely adopted in the reduction of metal oxides to their metallic states,[23,24] surface modification of various materials,[25–27] as well as etching processes in the semiconductor industry.[28,29] It also serves as an effective method for hydrogen doping in materials like TiO_2,[30–32] Si_3N_4,[33–35] and IGZO[36] without altering the mesostructure of the film. In this work, we demonstrate an H-3TM that operates through the reversible proton doping/extraction between a WO_x channel and a hydrogen-plasma-treated SiN_x electrolyte. The doping of protons using hydrogen plasma treatment allows wafer-scale device fabrication, and it does not involve any high temperature or wet processes. Tungsten oxides are commonly selected as the channel material because they are effective proton hosts, with the x value in H_xWO_3 reaching up to 0.5.[37] The conductance of the WO_x can be adjusted by altering the proton concentration within the material. The protons act as n-type dopants, introducing charge-balancing electrons into the conduction band through an outer circuit.[18,20,38,39] The device reveals linear potentiation/depression with a big dynamic range, long retention, and low variation, hence demonstrating high synaptic performance. Furthermore, 256 non-overlapping conductance states are obtained with the conductance increasing monotonically with continuous potentiation pulses.

2. Results and Discussion

As shown in the schematic in Figure S1 (Supporting Information), the hydrogen plasma treatment process is carried out using two power sources: the inductively coupled plasma (ICP) power generates the hydrogen plasma, while the reactive ion etching (RIE) power creates an electric field that accelerates protons for anisotropic implantation into the SiN_x film. Here, the surface of the SiN_x is exposed to the hydrogen plasma for 30 s prior to the deposition of the WO_x layer. A schematic of the proposed H-3TM is depicted in **Figure** 1a. It consists of a WO_x channel and a SiN_x electrolyte layer, with hydrogen-doped SiN_x ($H{:}SiN_x$) at the SiN_x/WO_x interface serving as the reservoir of active ions. Both the channel and electrolyte layers are in the amorphous phase according to the X-ray diffraction (XRD) patterns, in which only the peaks from the substrate were detected, as depicted in Figure S2 (Supporting Information). Due to the low conductance of the WO_x channel, a short channel length is crucial to ensure the detectable base channel conductance (G_0) at low reading voltages. Top-view optical image and the scanning electron microscope (SEM) image of the device are shown in Figure 1b, where the distance between the source and drain is ≈200 nm. The device has an effective switching area of 0.2 µm × 10 µm (length × width). A cross-sectional view of the device was obtained using focused ion beam (FIB) milling followed by transmission electron microscopy (TEM), as shown in Figure 1c. A protective Au layer was deposited on the top surface during FIB sample preparation to prevent charge accumulation. Elemental mapping was performed using energy-dispersive X-ray spectroscopy (EDS), and the results are presented in Figure 1d. Figure 1e shows the change in elemental atomic fractions along the depth direction, as indicated by the red arrow in Figure 1c. The combined cross-sectional imaging and EDS analyses clearly reveal the internal structure and material distribution within the device.

To verify the presence of protons on the surface of SiN_x, X-ray photoelectron spectroscopy (XPS) characterization was conducted on SiN_x samples both with and without hydrogen plasma treatment (Figure 1f,g). From the XPS spectra of pristine SiN_x, it can be detected that N is mainly coordinated by Si. The formation of the Si-O bonds in the Si spectra can be attributed to the surface oxidation when the sample is exposed to the air.[34] After being treated with hydrogen plasma, the coordination environment of N and Si is modified, characterized by the emergence of spectral peaks related to N-H and Si-H.[40] Hydrogen plasma contains large amounts of electrons and hydrogen species in various states (e.g., H^-, H^+, H^{2+}, H^{3+}).[23,41] Thus, negatively charged N in pristine SiN_x may donate electrons to those H clusters with positive valences. Given the higher electronegativity of H (2.2) compared to Si (1.9), electrons have a greater affinity toward H, thereby lowering the electron density of N and further enhancing the bonding energy of the N 1s electrons.[42] For Si, the negatively charged H clusters participate in the coordination. Since H has lower electronegativity than both O and N, the newly formed Si—H bonds exhibit the weakest bonding energy.[43] Overall, the presence of Si—H and N—H bonds affirms the successful introduction of protons into the SiN_x by the hydrogen plasma treatment. Furthermore, time-of-flight secondary ion mass spectrometry (TOF-SIMS) analysis was carried out on planar samples comprising a $WO_x/SiN_x/W$ stack to investigate hydrogen distribution. As shown in Figure S3 (Supporting Information), hydrogen depth profiles in the SiN_x layer are displayed for samples with and without hydrogen plasma treatment. The treated sample exhibits a notably higher hydrogen concentration, especially near the surface, confirming effective hydrogen incorporation as discussed. The SIMS profiles were normalized point-by-point using the total intensity of SiN^-, SiO^-, and $SiON^-$ secondary ion signals.

In addition to the XPS characterization of the standalone SiN_x film, depth profiling was performed on the WO_x/SiN_x bilayer using three etching cycles. Prior to the measurement, the etching rates for WO_x and SiN_x were calibrated to ensure accurate depth profiling—starting from the WO_x layer, proceeding through the interface, and finally into the SiN_x layer, as illustrated in Figure S4 (Supporting Information). The raw XPS spectra for W, O, Si, and N at these three etching cycles, comparing devices with and without hydrogen plasma treatment, are provided in Figures S5–S8 (Supporting Information). The etching cycle-atomic concentration profiles for different elements, i.e., W, O, Si, and N at the bulk WO_x, WO_x/SiN_x interface, and bulk SiN_x can be found in Figure 1h. After the hydrogen plasma treatment, there is a noticeable increase in the oxygen content across the WO_x/SiN_x interface, along with a decrease in the nitrogen content. Such a phenomenon can be explained by the high activity of the doped H in the $H{:}SiN_x$. The incorporation of protons introduces additional unsaturated bonds in the $H{:}SiN_x$, making the surface more prone to being oxidized during the reactive sputtering deposition process of the WO_x.[34] This observation is consistent with the EDS results, which reveal a denser oxygen distribution near the surface of SiN_x layer. While there might be a contribution from oxygen ion exchange between the WO_x and the surface-oxidized SiN_x layer, TOF-SIMS analysis confirms a high hydrogen

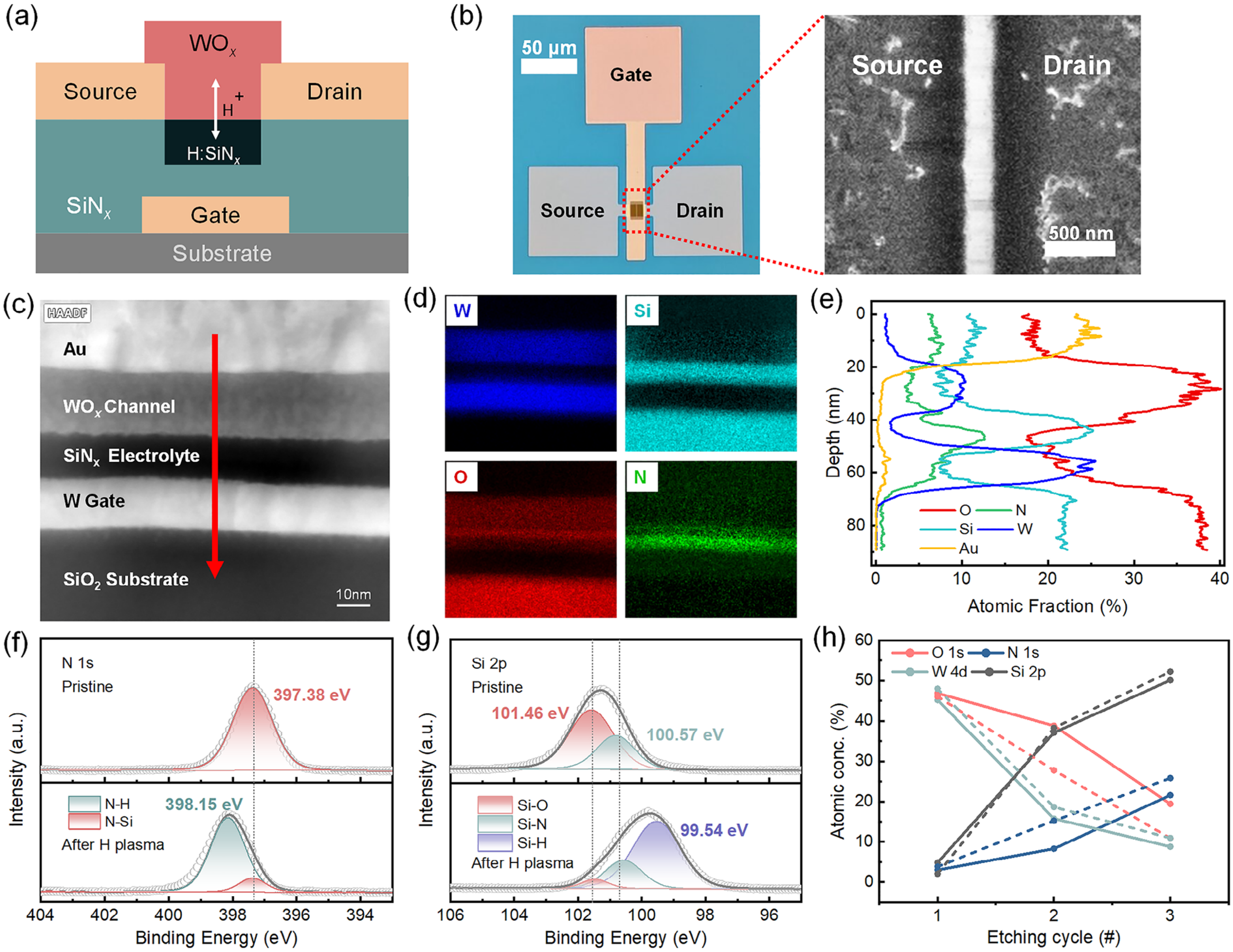

Figure 1. a) Schematic illustration of the proposed H-3TM device. b) Top-view optical image and SEM image of the device. The distance between the source and drain is ≈200 nm. c) Cross-sectional TEM image of the device, where the red arrow indicates the direction of the line scan. d) EDS elemental mapping of O, W, Si, and N. e) EDS line scan profile along the direction indicated in (c). f) XPS spectra of N 1s and g) Si 2p for SiN_x film with and without hydrogen plasma treatment. h) The etching cycle-atomic concentration profiles for different elements at the WO_x/SiN_x bilayer interface. The solid line and dashed line represent SiN_x with and without hydrogen plasma treatment, respectively.

concentration near the interface, indicating that only a portion of the Si—H and N—H bonds are oxidized. XPS depth profiling further shows that oxygen is already present at the interface even without hydrogen plasma treatment, and only a slight increase (≈10%) in oxygen content is observed after treatment. Notably, no switching behavior is observed in devices without hydrogen plasma treatment, suggesting that the contribution from oxygen ions in the plasma-treated device is minimal or negligible. Given the smaller size and lower mass of protons, as well as the lower bond dissociation energy of Si—H (3.09 eV) compared to Si—O (8.27 eV), the switching mechanism is predominantly contributed by proton migration.[44]

DC sweeps were performed for the gate and channel using the gate/source and drain/source configurations, respectively. The data is plotted on a log-linear scale as depicted in Figure S9 (Supporting Information), with a linear scale inset for reference. Compared to the gate leakage current, the current flow through the channel is three orders of magnitude higher. This suggests that the undoped bulk of SiN_x acts as a highly insulating gate dielectric, effectively suppressing the gate leakage current. The negligible gate leakage current allows an accurate reading of the channel conductance, minimizing errors or noise and leading to stable device switching performance. Application of a positive gate pulse induces proton migration from $H{:}SiN_x$ into the WO_x channel, causing a redox reaction that increases the conductance of WO_x as follows:[45]

$$WO_x + yH^+ + ye^- \leftrightarrow H_yWO_x \tag{1}$$

Conversely, the conductance is decreased when a negative gate pulse is applied. This change in conductance is analogous to the weight-updating behavior of a biological synapse. Thus, both potentiation and depression (P/D) can be emulated with positive and negative gate pulses, respectively.

In **Figure 2a**, the P/D processes under 32, 64, 128, and 256 pulses with identical potentiation pulses (5 V, 50 μs) and

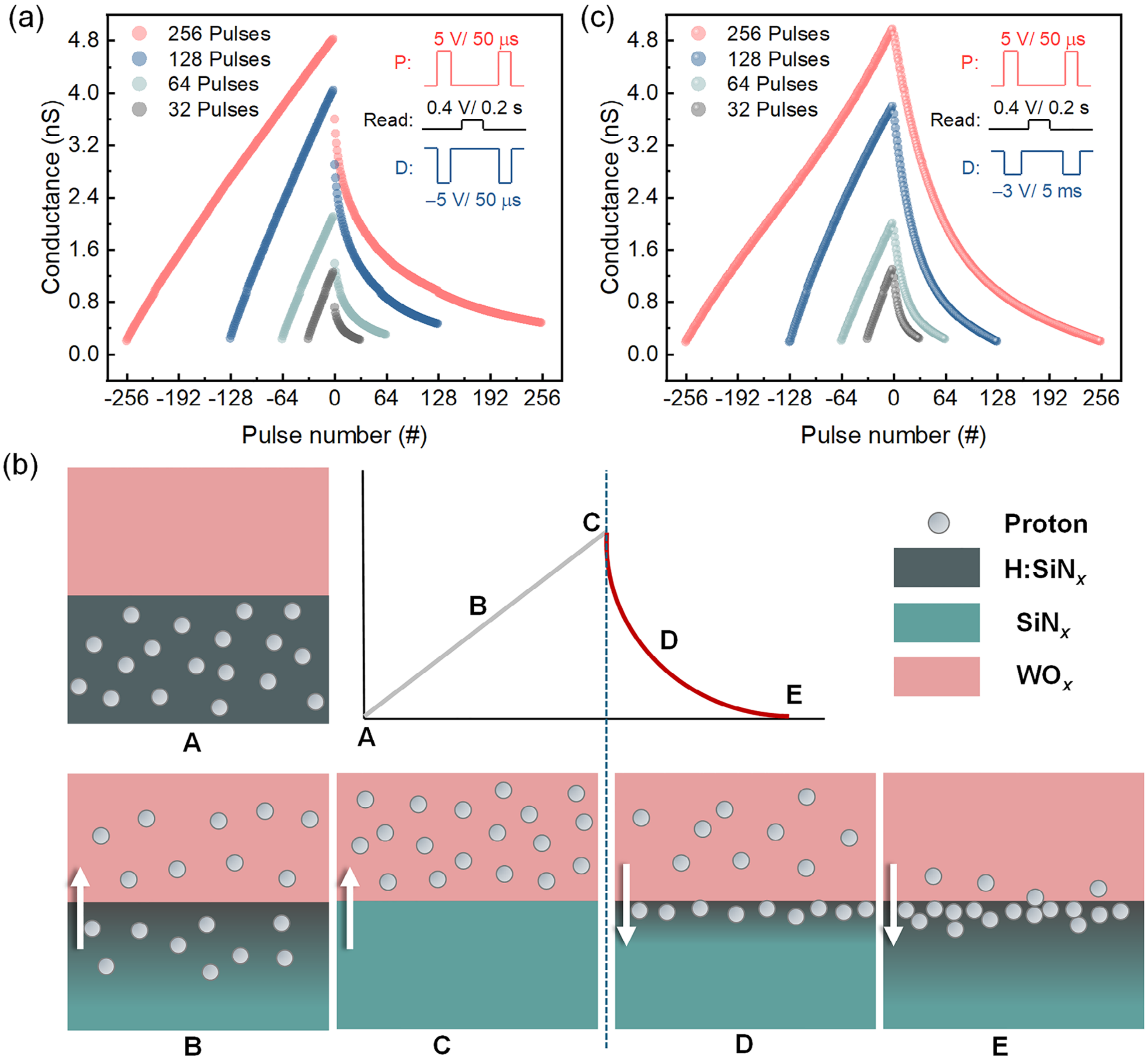

Figure 2. a) P/D performance with different numbers of applied pulses, where the pulse durations for both potentiation and depression processes are the same. b) Schematic of ion distribution near the interface during the P/D processes. The uniform diffusion of extracted protons throughout the SiN$_x$ is hindered by the low ion mobility in SiN$_x$. This accumulation of ions hinders subsequent ion extraction from the channel, leading to saturation in conductance modulation. c) P/D performance with different numbers of applied pulses, where the pulse duration for the depression process is longer. The reading process for (a) and (b) was carried out with a low drain voltage of 0.4 V.

depression pulses (−5 V, 50 µs) to the gate terminal were demonstrated. Here, the rise/fall time for each pulse is set to be 1 µs. After each programming pulse, the conductance of the channel is read out by a small drain voltage pulse (0.4 V, 0.2 s). It can be seen that the dynamic range, i.e., the ratio of the highest to lowest conductance (G_{max}/G_{min}), increases with the number of programming pulses applied to the device. It demonstrates a potentiation process with excellent linearity, while exhibiting significantly less linear depression characteristics with a pronounced initial conductance drop. After the initial drop, the reduction in conductance triggered by each pulse gradually becomes saturated. This can be attributed to the different proton mobility in SiN$_x$ and WO$_x$. The diffusion coefficient of protons in amorphous WO$_x$ ranges from 10^{-11} to 10^{-10} cm^2 sec^{-1}, which is several orders of magnitude greater than that within SiN$_x$ films.[46,47] The ion distribution near the interface during the P/D processes is illustrated in the schematic of Figure 2b. The migration of protons can be divided into three parts: migration within the bulk WO$_x$, across the WO$_x$/SiN$_x$ interface, and through the bulk SiN$_x$. There may also be an intermixing layer at the interface, and once the protons reside at this interface, they no longer contribute to the channel conductance. When the first depression pulse is applied,

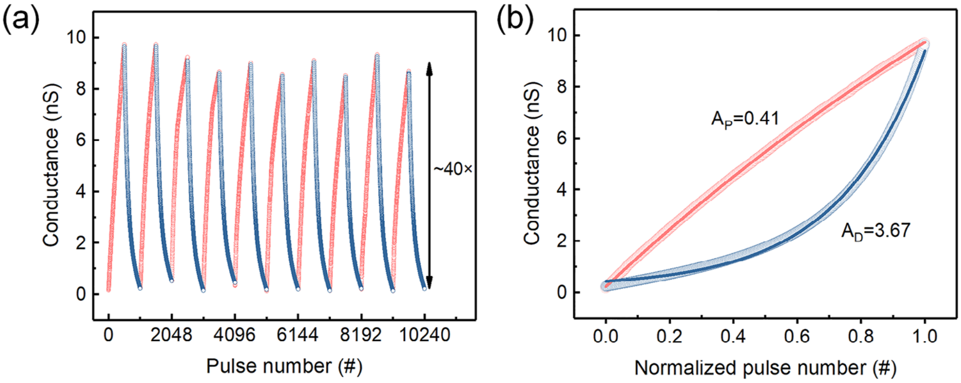

Figure 3. a) 10 P/D cycles with 512 pulses for both potentiation and depression processes. The obtained average dynamic range is ≈40. b) Nonlinearity analysis for one of the P/D curves with an A_P of 0.41 and an A_D of 3.67.

a large number of protons are extracted from the WO_x, contributing to the initial drop in conductance. Those protons accumulate in the SiN_x near the WO_x/SiN_x interface because the uniform diffusion of these protons throughout the SiN_x is hindered by the low ion mobility in SiN_x. This accumulation of ions hinders subsequent ion extraction from the channel, leading to saturation in conductance modulation.[3,5] Thus, by adopting pulses with lower amplitude but longer pulse duration, it should provide a lower electric field to avoid excessive initial proton extraction and allow further proton diffusion to prevent local ion accumulation. The P/D processes under potentiation pulses (5 V, 50 µs) and longer depression pulses (−3 V, 5 ms) with different numbers of programming pulses are depicted in Figure 2c. The initial drop during depression is significantly reduced, with a more symmetrical and linear weight-updating behavior obtained.

To quantitatively evaluate the linearity of the P/D curves, the data are fitted with the following behavioral model:[48,49]

$$G_P = G_{min} + B\left(1 - e^{-AP}\right) \tag{2}$$

$$G_D = G_{max} - B\left(1 - e^{A(P-1)}\right) \tag{3}$$

$$B = \frac{G_{max} - G_{min}}{1 - e^{-AP_{max}}} \tag{4}$$

in which G_{min} and G_{max} are extracted from the measured data. P_{max} is the number of pulses required to switch the channel conductance between G_{min} and G_{max}.The value of A indicates the nonlinearity of the weight-updating behavior, while B scales to match the range of G_{min} and G_{max}. To fit the model, the number of applied pulses was normalized, and the conductance states along the depression curve were mirrored back. For the perfectly ideal P/D curve, the value of A is 0. The nonlinearity fitting of the P/D curves from 50 µs-depression pulses and 5 ms-depression pulses is plotted in Figure S10a,b (Supporting Information). Table S1 (Supporting Information) shows the comparison between the two modes of depression pulses under different numbers of programming pulses. The 5 ms-depression pulse yields better overall nonlinearity factors (3.64–3.69) compared to the 50 µs-depression pulse (4.10–8.41).

Under the longer depression pulse scheme, an endurance test of the device was performed with more than 10^4 pulses, including 512 pulses for each potentiation and depression process. As shown in **Figure 3**a, an average dynamic range of ≈40 was achieved. A larger dynamic range (>10) is desirable because it enhances the accuracy of the synaptic weights mapping.[50,51] The devices with relatively smaller dynamic ranges are not only more vulnerable to noise but also lead to a deterioration in overall training performance.[52,53] The nonlinearity fitting was also performed for the P/D curves shown in Figure 3a. As an example, a nonlinearity factor of 0.41 for potentiation (A_P) and 3.67 for depression(A_D) was obtained from one of the cycles, as illustrated in Figure 3b. To assess cycle-to-cycle variation, the nonlinearity factor A over 10 cycles is summarized in Figure S11 (Supporting Information). The values of A exhibit a uniform distribution, with A_P consistently below 1 and A_D ≈3.6.

Additionally, the device demonstrates exceptional energy efficiency, with an energy consumption per write operation of ≈73 fJ, approaching the energy consumption of biological synapses per synaptic event (≈10 fJ).[54] Due to the highly insulating undoped SiN_x bulk layer, the gate current (I_G) during each pulse application period is extremely low and falls below the detection range of the Pulse-IV module of the analyzer. The gate resistance remained unchanged throughout the operation, thus, to estimate the power consumption, a DC sweep from 0 to 10 V was performed on five devices, as shown in Figure S12 (Supporting Information). The averaged I_G value at 5 V was then multiplied by the voltage amplitude and pulse duration during the writing operation.

Beyond analog switching with multiple conductance states, the retention of each state is crucial for synaptic devices to store and recall information accurately without degradation. Using the same pulse condition (5 V, 50 µs) as in the P/D performance measurements, twenty conductance states covering a wide dynamic range were obtained by applying varying numbers of pulses, and their retention was monitored for 1500 s, as shown in **Figure 4**a. After 1500 s, the drifts in conductance among these 20 conductance states were negligible, with the largest degradation being only ≈2.8% from the conductance level measured right after the programming. This long retention ensures a stable, low-power operation in neuromorphic systems, particularly for applications requiring reliable long-term memory, adaptive learning, and continuous operation.[12,55,56] In contrast to reported 3TMs where the unwanted conductance drift is always from higher

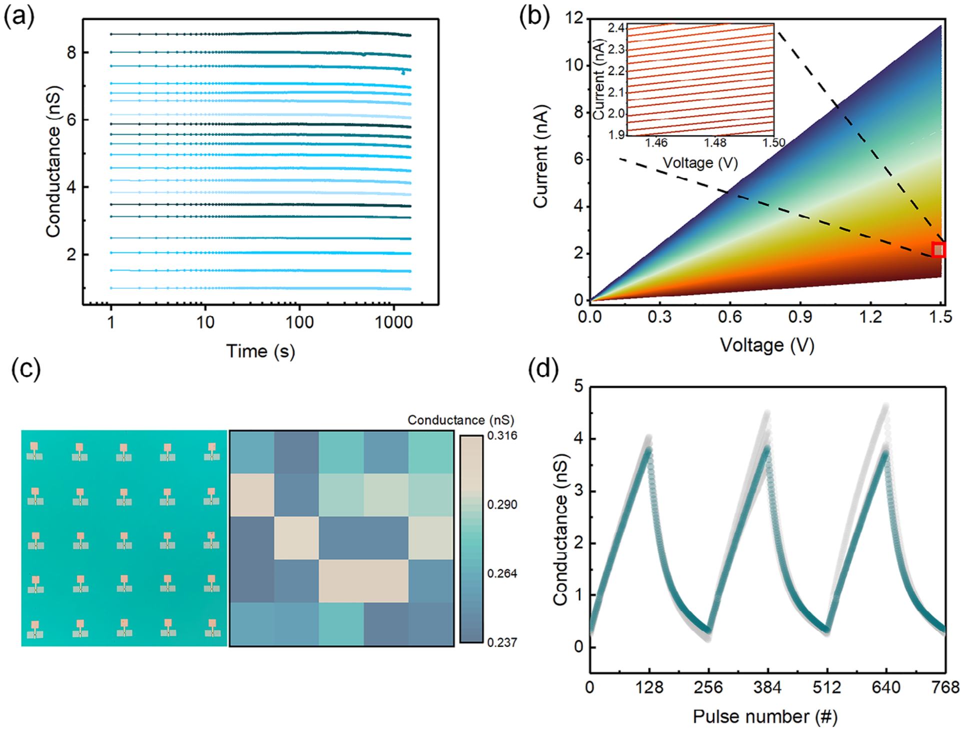

Figure 4. a) The measured retention of 20 selected conductance states, where the degradation of each state is very minimal over 1500 s. b) I-V plots of 256 monotonically potentiated states, demonstrating good I–V linearity and wide range programmability. The enlarged figure shows clear non-overlapping of each state. c) Optical image of the sample with 25 devices and the spatial mapping of G_0 across all devices. d) Three P/D cycles obtained from five different devices.

to lower conductance, the conductance drift in the proposed H-3TM is different.[2,8,11,57] Here, the conductance programmed by a potentiation pulse initially decreases before stabilizing. Conversely, conductance set by a depression pulse first increases and then stabilizes, as depicted in Figure S13 (Supporting Information). This retention behavior is potentially due to incomplete proton migration and accumulation at the interface. Once the pulse stimuli are removed, the protons at the interface (prior to crossing the interface) will stay in the same layer and get redistributed by the local gradient concentration of protons through diffusion, resulting in a small opposite change of conductance.

Figure 4b shows the I-V plot for 256 conductance states obtained through 256 potentiation pulses, during which conductance increased in a uniform and monotonic manner. After each pulse, a voltage sweep from 0 to 1.5 V was applied to read the programmed state, revealing the ohmic I-V property of the WO_x channel. The inset in Figure 4b is the enlarged view of the conductance, which clearly shows no overlapping between adjacent states. During inference, vector-matrix multiplication (VMM) is performed to generate predictions by transforming the input based on the trained weights of each synaptic device. In conventional two-terminal memristors, I-V linearity is typically observed only in high-conductance states, while low-conductance states tend to exhibit nonlinear and unpredictable behavior. This nonlinearity can distort VMM operations, as the output current may no longer accurately represent a simple weighted sum of the inputs.[58–60] The ohmic I-V characteristic of the H-3TM enables constant conductance regardless of the applied voltage, preserving the VMM accuracy with a precise linear combination of the input voltages and conductance values.

To examine the device-to-device variation of the 3TMs, the G_0 of 25 devices on the as-fabricated sample was measured to be ≈0.3 nS, as spatially mapped in Figure 4c. The good uniformity on the wafer scale is owing to the hydrogen plasma-enabled proton doping method. Additionally, three cycles from 5 devices with 128 P/D pulses were obtained to evaluate the uniformity of the switching behavior, as shown in Figure 4d. The coefficient of variation (CoV) for cycle-to-cycle and device-to-device variations in each conductance state is calculated to range from 1.5% to 19.2% and 2.3% to 24.0%, respectively. As shown in Figure S14 (Supporting Information), the CoVs of the low conductance states are relatively higher than those of the high conductance states, which can be attributed to the difference in the pristine device conductance. It is also observed that the potentiation process shows better uniformity compared to that of the depression process, consistent with its higher linearity. Similarly, the P/D curves in Figure 4d were fitted using the nonlinearity model, exhibiting consistent values of A across different devices and cycles, as illustrated in Figure S15 (Supporting Information). The superior reproducibility and consistency across devices and over repeated cycles shown in Figure 4d allow a more reliable, accurate, and efficient operation of the device.

To further understand the charge carrier transport mechanism, the proton migration across the WO_x/ SiN_x interface is investigated through molecular dynamics (MD) simulation.[61] **Figure 5a–c** shows the schematics of the interface under different

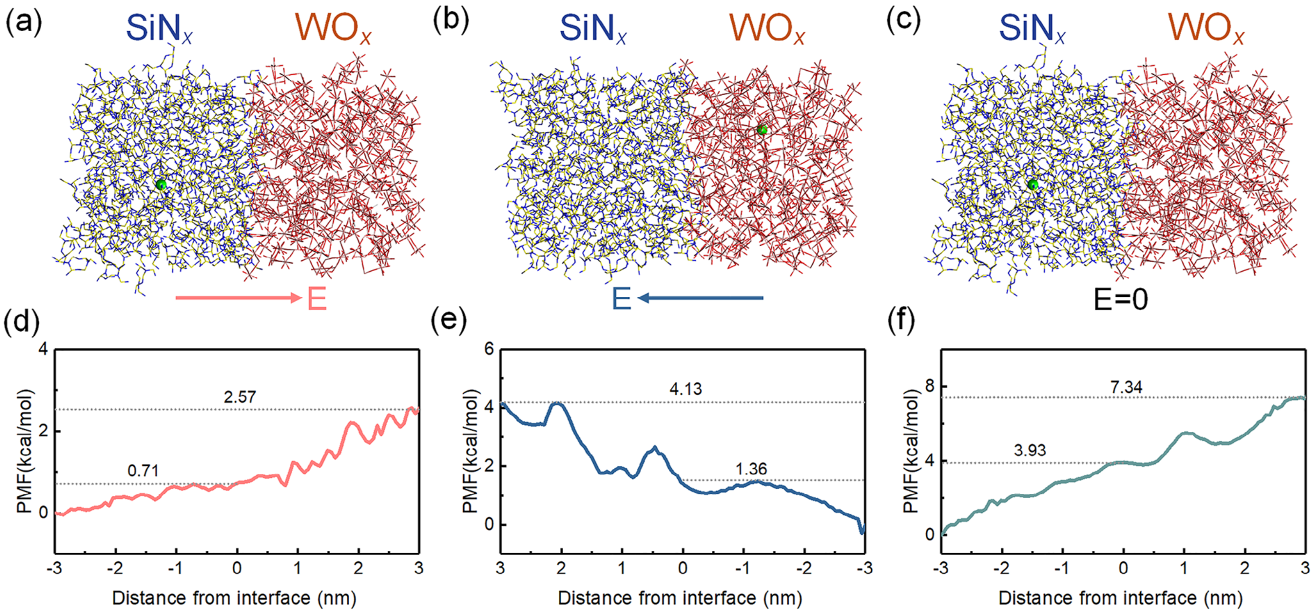

Figure 5. Simulation of proton migration at the WO$_x$/SiN$_x$ interface when a) an electric field is applied from SiN$_x$ to WO$_x$, b) an electric field is applied from WO$_x$ to SiN$_x$, and c) without the external electric field. d–f) PMF for a proton to move across the interface for conditions in a–c), respectively.

electric fields, while Figure 5d–f displays the required potential of mean force (PMF) for a single proton to cross the interface as a function of distance. As shown in Figure 5a, when an electric field is applied with orientation from the SiN$_x$ to the WO$_x$, the PMF for a single proton to diffuse across the interface is ≈0.71 kcal mol^{-1}. Conversely, when the direction of the electric field is reversed (Figure 5b), a higher PMF is required for proton migration across the interface (1.36 kcal mol^{-1}), indicating a higher energy barrier for the proton to penetrate the regions of the SiN$_x$ distant from the boundary (4.13 kcal mol^{-1}). These simulation results are consistent with our experimental observations, where the slow proton diffusion in the SiN$_x$ leads to proton accumulation, hindering further proton injection. The PMF for the migration of a proton from the SiN$_x$ to the WO$_x$ without an external electric field was simulated, as presented in Figure 5c. The direction was chosen because protons have a relatively direct migration into the WO$_x$. The required driving force for the transport of a proton through the interfacial site is 3.93 kcal mol^{-1}, and for deeper infiltration, it is 7.34 kcal mol^{-1}. This result supports the high retention performance of the device, where the protons exhibit a strong tendency to remain in SiN$_x$ rather than shuttling toward WO$_x$.

To assess the performance of the proposed H-3TM as a synaptic device, a supervised pattern recognition simulation was performed using a fully connected multilayer perceptron neural network. This network includes an input layer with 784 neurons, a hidden layer with 300 neurons, and an output layer with 10 neurons. Each neuron is fully connected to the neurons in the neighboring layer by a synapse whose weight is emulated by the conductance of the device, as shown in **Figure 6a**. The training involved 28 × 28-pixel grayscale images of handwritten digits from the Modified National Institute of Standards and Technology (MNIST) database, as well as images of clothing from the Fashion-MNIST (F-MNIST) dataset.[62,63] The latter dataset is more challenging and less frequently used than the MNIST dataset, due to its greater complexity and nonlinear classification problems.[64] During the training, the weight of each synapse was adjusted based on the linearity, dynamic range, precision, and device-to-device variation depicted in Figure 4d. After 50 epochs, the H-3TM achieved recognition accuracy of 93.7% for the MNIST dataset and 82.0% for the F-MNIST dataset as plotted in Figure 6b,c, respectively. For comparison, a simulation using an ideal synaptic device with perfect linearity ($A_P = A_D = 0$), infinite dynamic range, unlimited conductance states, and zero variation was carried out, reaching an accuracy of 96.5% and 82.4% for MNIST and F-MNIST datasets, respectively. The obtained accuracy of the H-3TM is comparable to the ideal case, which is attributed to its multiple conductance states and minimal variation in conductance modulation. The same simulation was also conducted with the P/D cycles presented in Figure 2a,b. As plotted in Figures S16 and S17 (Supporting Information), the recognition accuracies with the shorter pulse scheme are consistently lower for both MNIST and F-MNIST datasets. Moreover, the evolution of the accuracies under the shorter pulse scheme exhibits greater fluctuation when using the MNIST dataset, due to the inaccessible conductance states arising from significant drops during the depression processes. In addition to training, inference was performed using the trained neural network while considering device variations.[65,66] The inference accuracy obtained based on the H-3TM performances was evaluated against the ideal case, revealing a difference of less than 0.5% for both the MNIST and F-MNIST datasets, as shown in Figure 6d. In addition to the MNIST and F-MNIST datasets, the device's synaptic performances were further evaluated using more complex CIFAR-10 and CIFAR-100 datasets. CIFAR-10 contains 60 000 32 × 32 color images across 10 classes, while CIFAR-100 comprises 100 classes with 600 images per class.[67] Due to the complexity of these datasets, the neural network architecture used for simpler

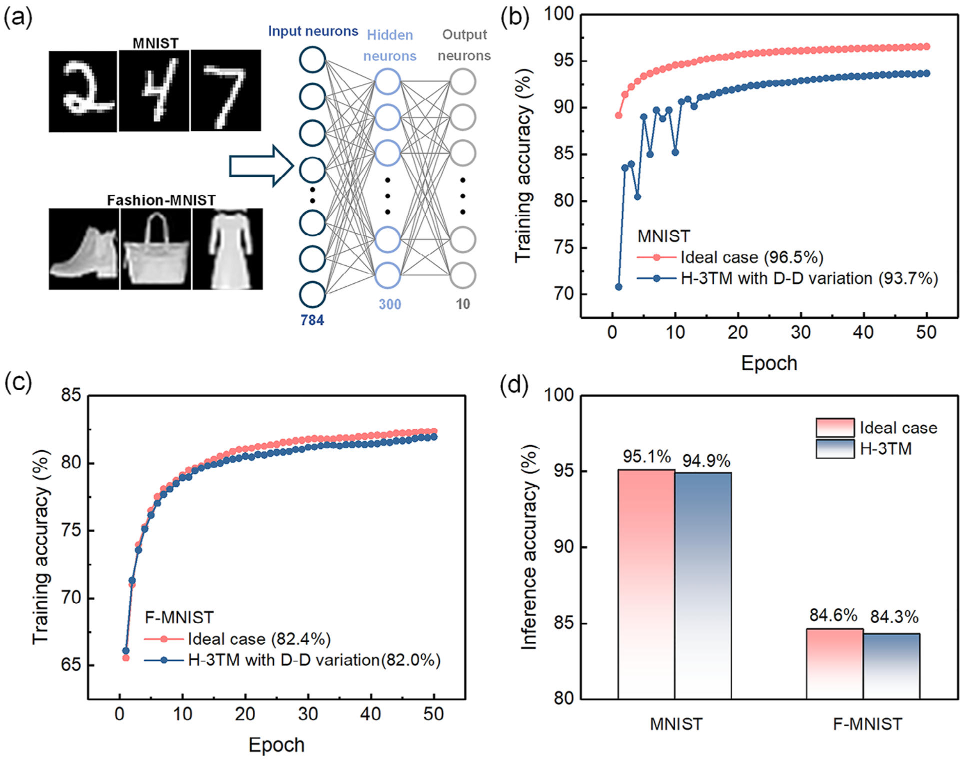

Figure 6. a) Architecture of the custom neural network trained for pattern recognition tasks, which involves a dedicated training process. Sample images from the MNIST and F-MNIST datasets are displayed on the left. Training accuracy of the neural network is shown for b) MNIST and c) F-MNIST datasets, comparing results based on the H-3TM model and the ideal numerical case. d) Inference accuracy obtained using the trained neural network based on the H-3TM and the ideal case, with a difference of less than 0.5% for both MNIST and F-MNIST datasets.

datasets was unsuitable for capturing their rich features. Instead, a well-established RESNET-56 architecture was utilized, where the "56" corresponds to the total number of convolution layers within the deep neural network. RESNET incorporates multiple skip connections, which bypass less significant layers, to mitigate training accuracy loss in deep architectures. Inference was performed using the pre-trained RESNET-56 network on CIFAR-10 and CIFAR-100.[66,68] The resulting accuracies deviated by only 1.9% and 2.4% from the ideal case, respectively, as shown in Figure S18 (Supporting Information).

Lastly, a comparison with all reported CMOS-compatible H-3TMs is provided in Table S2 (Supporting Information), highlighting that our device is the first to use hydrogen plasma in this field. This approach enables more direct and uniform proton doping, and the device also exhibits outstanding synaptic performance.

3. Conclusion

In this work, an H-3TM that functions via the reversible doping and extraction of protons into a WO_x channel from a hydrogen plasma-treated SiN_x electrolyte is presented. This method of engineering a proton source with hydrogen plasma enables the fabrication of the devices on a wafer scale without the need for high-temperature processes or wet chemistry. The device showcases excellent synaptic characteristics, such as highly linear potentiation and depression behavior with a considerably large dynamic range of up to 40, non-overlapping conductance states with ohmic channel properties, as well as high retention performance and relatively low variation among devices. MD simulations were conducted to investigate the asymmetric conductance change during the P/D process, where the energy required for the proton to migrate across the interface from WO_x to SiN_x is higher compared to that of the reversed process. The variations among devices and switching cycles were included in the pattern recognition simulation, yielding an accuracy of 82.0% (compared to 82.4% under ideal conditions) when using the complex F-MNIST dataset. Overall, the results presented in this work demonstrate that the H-3TM is a promising candidate for hardware implementation of artificial neural networks.

4. Experimental Section

Device Fabrication: The H-3TM was fabricated on a SiO_2/Si substrate with a bottom gate and top channel configuration. First, the gate electrode was patterned and deposited with 15 nm of W by DC sputtering at a power of 50 W. Next, 20-nm SiN_x was blanket deposited in a Plasma-Therm 200 mm Plasma Enhanced Chemical Vapor Deposition (PECVD) system. The temperature and pressure in the PECVD chamber were 280 °C and 600 mTorr. After this, the SiN_x above the big pad of the gate was then etched in a Plasma-Therm 200 mm ICP-RIE system to form a gate-access via. Next, the source and drain patterning was performed with a well-calibrated electron beam dose to form the shortest distance. 10 nm of W was deposited to form the source and drain pads. Subsequently, the pattern of the channel was formed. Before the deposition of the WO_x channel, the sample was treated with 30 s of hydrogen plasma (inductively coupled plasma power: 600 W, RF bias power to accelerate the plasma ions: 600 W) in a ULVAC Entron EX 300 mm physical vapor deposition system. The sample was immediately transferred into the sputtering chamber, and a 20 nm-WO_x layer was deposited by reactive sputtering from a W target with the Ar: O_2 ratio of 7:3. The fabrication processes are illustrated in Figure S19 (Supporting Information). All the patterning processes during the fabrication of the device are performed with a Raith e-line electron beam lithography (EBL). In the EBL process, a positive AR-P 6200 e-beam resist was spin-coated and soft-baked at 150 °C for 1 min. All sputtering processes were executed with an AJA International ATC-Orion 8-target UHV magnetron sputtering deposition system, and the sputtering condition was fixed at room temperature under a pressure of 2 mTorr and a power of 50 W.

Device and Film Characterization: All electrical properties of the device were measured in an ambient at room temperature with a Keithley 4200A SCS parameter analyzer. The XPS was performed using an AXIS Supra spectrometer equipped with a monochromatic Al Kα source. Depth profiling was carried out using an Ar Gas Cluster Ion Source (GCIS, Minibeam 6) operated at 5 keV with a raster size of 2×2 mm^2. This GCIS method was chosen over conventional monatomic Ar^+ sputtering to minimize surface damage and preserve the chemical integrity of the sample during etching. Etching time was carefully adjusted to target the depths of interest. Precautions were taken to reduce charging and ensure measurement accuracy, including electrical grounding of the sample. TEM sample preparation was performed using a Helios 600 FIB system. Imaging was conducted with a 5 keV field emission gun electron beam. Ga^+ ions were used for milling, with specimen cutting and cleaning carried out at 30 and 2 keV, respectively. Subsequent TEM analysis was conducted using a Talos F200X G2 microscope operated at 200 kV. The energy spread was 0.4 eV, and the spatial resolution was 0.12 nm in TEM mode and 0.16 nm in STEM mode. Elemental mapping was performed using four SuperX EDS detectors with a total solid angle of 0.9 sr. TOF-SIMS measurements were conducted using a TOF-SIMS.5 instrument under a base pressure of 3.6×10^{-8} mbar. A 2 keV Cs^+ sputtering ion beam (70 nA current) was used to etch a 300 µm × 300 µm area, while a pulsed Bi^{1+} primary analysis beam (13.3 ns pulse width, 30 keV energy, 3 pA current) was scanned over a 100 µm × 100 µm area. Depth profiles were acquired in interlaced mode, where negative ion polarity analysis was conducted immediately following Cs^+ sputtering on the same surface.

MD Simulation: Atomistic molecular dynamics simulations have been performed in the GROMACS (version 2020.6) simulation package using the Universal force field, which covers elements in the whole periodic table. The amorphous interface was built by melting the crystal structures of $H(WO_3)_4$ and $H{:}Si_3N_4$, annealing from high temperatures to room temperature. Equilibration of the interface was performed for 10 ns, and two hydrogen were picked for later free energy calculations through the PMF method. The PMF calculations were performed by pulling one hydrogen from one phase to the other under two different static electric field directions from one phase to the other or no electric field, through the umbrella sampling mechanism with a pulling force constant of 100 $\mathrm{kCal \cdot mol^{-1} \cdot nm^{-2}}$ under the NVT ensemble. After the pulling process, 30 configurations were generated and sampled for 5 ns, while taking the last 2 ns for analysis of the free energy integration using the g_wham program. An integration time-step of 1 fs was used, and the temperature was coupled to 298 K using the Nose-Hoover method. A cutoff scheme of 1.2 nm was used for the nonbonded interactions, and the Particle Mesh Ewald method with a Fourier spacing of 0.1 nm was applied for the long-range electrostatic interactions. All covalent bonds with hydrogen atoms were constrained using the LINCS algorithm.

Supporting Information

Supporting Information is available from the Wiley Online Library or from the author.

Acknowledgements

This work was supported by a RIE2020 ASTAR AME IAF-ICP Grant (No. I1801E0030). The authors appreciate Shenzhen HUASUAN Technology Co., Ltd., China, for performing the MD simulation.

Conflict of Interest

The authors declare no conflict of interest.

Data Availability Statement

The data that support the findings of this study are available from the corresponding author upon reasonable request.

Keywords

hydrogen plasma, memristor, protonic, synaptic device, three-terminal

Received: March 5, 2025
Revised: April 26, 2025

---

[1] H. H. Kwak, N. Kim, S. Jeon, S. Kim, J. Woo, *Nano Converg.* **2024**, *11*, 9.
[2] L. Liu, P. A. Dananjaya, M. Y. Chee, G. J. Lim, C. X. X. Lee, W. S. Lew, *ACS Appl. Mater. Interfaces* **2023**, *15*, 29287.
[3] R. D. Nikam, J. Lee, K. Lee, H. Hwang, *Small* **2023**, *19*, 2302593.
[4] G. Ding, H. Li, J. Y. Zhao, K. Zhou, Y. Zhai, Z. Lv, M. Zhang, Y. Yan, S. T. Han, Y. Zhou, *Chem. Rev.* **2024**, *124*, 12738
[5] M. Huang, M. Schwacke, M. Onen, J. del Alamo, J. Li, B. Yildiz, *Adv. Mater.* **2023**, *35*, 2205169.
[6] A. A. Talin, Y. Li, D. A. Robinson, E. J. Fuller, S. Kumar, *Adv. Mater.* **2022**, *35*, 2204771.
[7] J. Cui, F. An, J. Qian, Y. Wu, L. L. Sloan, S. Pidaparthy, J. M. Zuo, Q. Cao, *Nat. Electron.* **2023**, *6*, 292.
[8] L. Liu, P. A. Dananjaya, C. C. I. Ang, E. K. Koh, G. J. Lim, H. Y. Poh, M. Y. Chee, C. X. X. Lee, W. S. Lew, *Nanoscale* **2023**, *15*, 17076.
[9] E. K. Koh, P. A. Dananjaya, H. Y. Poh, L. Liu, C. X. X. Lee, J. R. Thong, Y. S. You, W. S. Lew, *Nanoscale Horizons* **2024**, *9*, 828.
[10] C. X. X. Lee, P. A. Dananjaya, F. Tan, E. K. Koh, L. Liu, K. Cheng, W. Yi, W. S. Lew, *ACS Appl. Electron. Mater.* **2025**, *7*, 1415.
[11] R. D. Nikam, M. Kwak, J. Lee, K. G. Rajput, H. Hwang, *Adv. Electron. Mater.* **2020**, *6*, 1901100.
[12] Y. Li, E. J. Fuller, S. Asapu, S. Agarwal, T. Kurita, J. J. Yang, A. A. Talin, *ACS Appl. Mater. Interfaces* **2019**, *11*, 38982.
[13] E. J. Fuller, F. El Gabaly, F. Léonard, S. Agarwal, S. J. Plimpton, R. B. Jacobs-Gedrim, C. D. James, M. J. Marinella, A. A. Talin, *Adv. Mater.* **2017**, *29*, 1604310.
[14] M. T. Sharbati, Y. Du, J. Torres, N. D. Ardolino, M. Yun, F. Xiong, *Adv. Mater.* **2018**, *30*, 1802353.
[15] Y. Li, E. J. Fuller, J. D. Sugar, S. Yoo, D. S. Ashby, C. H. Bennett, R. D. Horton, M. S. Bartsch, M. J. Marinella, W. D. Lu, A. A. Talin, *Adv. Mater.* **2020**, *32*, 2003984.
[16] C. Lee, K. G. Rajput, W. Choi, M. Kwak, R. D. Nikam, S. Kim, H. Hwang, *IEEE Electron Device Lett.* **2020**, *41*, 1500.
[17] J. Lee, R. D. Nikam, M. Kwak, H. Hwang, *IEEE Trans. Electron Devices* **2022**, *69*, 2218.
[18] X. Yao, K. Klyukin, W. Lu, M. Onen, S. Ryu, D. Kim, N. Emond, I. Waluyo, A. Hunt, J. A. del Alamo, J. Li, B. Yildiz, *Nat. Commun.* **2020**, *11*, 3134.

[19] R. D. Nikam, J. Lee, W. Choi, W. Banerjee, M. Kwak, M. Yadav, H. Hwang, *Small* **2021**, *17*, 2103543.
[20] M. Onen, N. Emond, J. Li, B. Yildiz, J. A. Del Alamo, *Nano Lett.* **2021**, *21*, 6111.
[21] M. Onen, N. Emond, B. Wang, D. Zhang, F. M. Ross, J. Li, B. Yildiz, J. A. Del Alamo, *Science* **2022**, *377*, 539.
[22] G. Ding, J. Y. Zhao, K. Zhou, Q. Zheng, S. T. Han, X. Peng, Y. Zhou, *Chem. Soc. Rev.* **2023**, *52*, 7071.
[23] K. C. Sabat, P. Rajput, R. K. Paramguru, B. Bhoi, B. K. Mishra, *Plasma Chem. Plasma Process.* **2014**, *34*, 1.
[24] A. Vesel, A. Drenik, R. Zaplotnik, M. Mozetic, M. Balat-Pichelin, *Surf. Interface Anal.* **2010**, *42*, 1168.
[25] A. Sasinska, T. Singh, S. Wang, S. Mathur, R. Kraehnert, *J. Vac. Sci. Technol. A* **2015**, *33*, 01A152.
[26] W. C. Tsai, S. J. Wang, C. L. Chang, C. H. Chen, R. M. Ko, B. W. Liou, *EPL* **2008**, *84*, 16001.
[27] Y. J. Huang, P. J. Yen, H. C. Wang, H. C. Chen, K. H. Wei, *Org. Electron.* **2019**, *72*, 6.
[28] Y. Iijima, T. Tazawa, K. Sato, M. Oshima, K. Hiraoka, *Surf. Interface Anal.* **2000**, *29*, 596.
[29] D. Hug, S. Zihlmann, M. K. Rehmann, Y. B. Kalyoncu, T. N. Camenzind, L. Marot, K. Watanabe, T. Taniguchi, D. M. Zumbühl, *npj 2D Mater. Appl.* **2017**, *1*, 21.
[30] Z. Wang, C. Yang, T. Lin, H. Yin, P. Chen, D. Wan, F. Xu, F. Huang, J. Lin, X. Xie, M. Jiang, *Adv. Funct. Mater.* **2013**, *23*, 5444.
[31] S. Z. Islam, A. Reed, S. Nagpure, N. Wanninayake, J. F. Browning, J. Strzalka, D. Y. Kim, S. E. Rankin, *Microporous Mesoporous Mater.* **2018**, *261*, 35.
[32] F. H. Wang, H. P. Chang, J. C. Chao, *Thin Solid Films* **2011**, *519*, 5178.
[33] M. Bouchilaoun, A. Soltani, A. Chakroun, A. Jaouad, M. Darnon, F. Boone, H. Maher, *Phys. Status Solidi. A* **2018**, *215*, 1700658.
[34] Y. Rui, M.-H. Chen, S. Pandey, L. Li, *J. Vac. Sci. Technol. A* **2023**, *41*, 022601.
[35] K. Nakane, R. H. J. Vervuurt, T. Tsutsumi, N. Kobayashi, M. Hori, *ACS Appl. Mater. Interfaces* **2019**, *11*, 37263.
[36] S. H. Yang, J. Y. Kim, M. J. Park, K. H. Choi, J. S. Kwak, H. K. Kim, J. M. Lee, *Surf. Coatings Technol.* **2012**, *206*, 5067.
[37] D. Nishioka, T. Tsuchiya, T. Higuchi, K. Terabe, *Neuromorphic Comput. Eng.* **2023**, *3*, 034008.
[38] A. W. Powell, A. Stavrinadis, S. Christodoulou, R. Quidant, G. Konstantatos, *Nano Lett.* **2020**, *20*, 3485.
[39] G. A. Niklasson, C. G. Granqvist, *J. Mater. Chem.* **2007**, *17*, 127.
[40] J. Kim, W. Jeong, S. Lee, S. Jeong, S. H. Ko Park, *J. Am. Ceram. Soc.* **2021**, *104*, 6670.
[41] S. Peng, W. Wu, H. Ren, J. Zhang, Y. Xu, A. Zhang, T. Zhang, T. Ma, Y. Jiang, J. Sun, J. Wen, Z. Guo, J. Chen, *Rev. Sci. Instrum.* **2019**, *90*, 123305.
[42] D. Bianchini, G. B. Galland, J. H. Z. Dos Santos, R. J. J. Williams, D. P. Fasce, I. E. Dell'Erba, R. Quijada, M. Perez, *J. Polym. Sci. Part A Polym. Chem.* **2005**, *43*, 5465.
[43] H. Braunschweig, P. Constantinidis, T. Dellermann, W. C. Ewing, I. Fischer, M. Hess, F. R. Knight, A. Rempel, C. Schneider, S. Ullrich, A. Vargas, J. D. Woollins, *Angew. Chem., Int. Ed.* **2016**, *55*, 5606.
[44] J. A. Dean, *Lange's Handbook of Chemistry*, McGraw-Hill Company, New York, **1999**.
[45] H. W. Park, B. G. Seo, J. W. Shim, N. Il Kim, Y. S. Choi, J. H. Shim, *Appl. Catal. B Environ.* **2023**, *337*, 122956.
[46] G. T. Yu, S. K. Yen, *Appl. Surf. Sci.* **2002**, *202*, 68.
[47] R. S. Crandall, B. W. Faughnan, *Appl. Phys. Lett.* **1975**, *26*, 120.
[48] G. Wu, C. Wan, J. Zhou, L. Zhu, Q. Wan, *Nanotechnology* **2014**, *25*, 094001.
[49] J. Tang, D. Bishop, S. Kim, M. Copel, T. Gokmen, T. Todorov, S. Shin, K. T. Lee, P. Solomon, K. Chan, W. Haensch, J. Rozen, in *IEEE Int. Electron Devices Meeting (IEDM)*, IEEE, Piscataway, NJ **2018**, pp. 13.1.1–13.1.4.
[50] S. Seo, J. J. Lee, H. J. Lee, H. W. Lee, S. Oh, J. J. Lee, K. Heo, J. H. Park, *ACS Appl. Electron. Mater.* **2020**, *2*, 371.
[51] Peng X., Huang S., Luo Y., Sun X., Yu S., in IEEE Int. Electron Devices Meet, IEEE, New Jersey **2019**, pp. 32.35.31–32.35.34.
[52] H. Lee, D. G. Ryu, G. Lee, M. K. Song, H. Moon, J. Lee, J. Ryu, J. H. Kang, J. Suh, S. Kim, J. Lim, D. Jeon, S. Kim, J. Kim, Y. S. Lee, *Adv. Electron. Mater.* **2022**, *8*, 2200378.
[53] S. Yu, *Proc. IEEE* **2018**, *106*, 260.
[54] K. Byun, I. Choi, S. Kwon, Y. Kim, D. Kang, Y. W. Cho, S. K. Yoon, S. Kim, *Adv. Mater. Technol.* **2022**, *8*, 2200884.
[55] D. S. Kim, V. J. Watkins, L. A. Cline, J. Li, K. Sun, J. D. Sugar, E. J. Fuller, A. A. Talin, Y. Li, *Adv. Electron. Mater.* **2023**, *9*, 2200958.
[56] J. Zhu, T. Zhang, Y. Yang, R. Huang, *Appl. Phys. Rev.* **2020**, *7*, 011312.
[57] G. Han, J. Seo, H. Kim, D. Lee, *J. Mater. Chem. C* **2023**, *11*, 5167.
[58] F. Cai, J. M. Correll, S. H. Lee, Y. Lim, V. Bothra, Z. Zhang, M. P. Flynn, W. D. Lu, *Nat. Electron.* **2019**, *2*, 290.
[59] D. Joksas, E. Wang, N. Barmpatsalos, W. H. Ng, A. J. Kenyon, G. A. Constantinides, A. Mehonic, *Adv. Sci.* **2022**, *9*, 2105784.
[60] A. Amirsoleimani, F. Alibart, V. Yon, J. Xu, M. R. Pazhouhandeh, S. Ecoffey, Y. Beilliard, R. Genov, D. Drouin, *Adv. Intell. Syst.* **2020**, *2*, 2000115.
[61] Z. Chen, T. Wang, Z. Wu, Y. Hou, A. Chen, Y. Wang, Z. Huang, O. G. Schmidt, M. Zhu, J. Fan, C. Zhi, *Nat. Commun.* **2024**, *15*, 3748.
[62] H. Xiao, K. Rasul, R. Vollgraf, *arXiv* **2017**, arXiv:170807747.
[63] M. A. Nielsen, *Neural Networks and Deep Learning*, Determination Press, San Francisco, CA, USA **2015**.
[64] Y. Li, T. P. Xiao, C. H. Bennett, E. Isele, A. Melianas, H. Tao, M. J. Marinella, A. Salleo, E. J. Fuller, A. A. Talin, *Front. Neurosci.* **2021**, *15*, 636127.
[65] V. Milo, F. Anzalone, C. Zambelli, E. Perez, M. K. Mahadevaiah, O. G. Ossorio, P. Olivo, C. Wenger, D. Ielmini, *Proc. from the Int. Reliability Physics Symp. (IRPS)*, IEEE, New York **2021**.
[66] E. K. Koh, P. A. Dananjaya, L. Liu, C. Xiu, X. Lee, G. J. Lim, Y. S. You, W. S. Lew, *ACS Nano* **2024**, *18*, 29602.
[67] CIFAR-10 and CIFAR-100 datasets, https://www.cs.toronto.edu/⟨kriz/cifar.html (accessed: December 2024).
[68] K. He, X. Zhang, S. Ren, J. Sun, presented at IEEE Conf. Computer Vision and Pattern Recognition (CVPR), Las Vegas, NV, USA, December, **2016**.